ACS APPLIED MATERIALS & INTERFACES

Research Article

www.acsami.org

Sandwiched ZnO@Au@Cu_2O Nanorod Films as Efficient Visible-Light-Driven Plasmonic Photocatalysts

Shoutian Ren,*[,†] Benyang Wang,[†] Hui Zhang,[‡] Peng Ding,[†] and Qiang Wang[†]

[†]Department of Optoelectronic Science, Harbin Institute of Technology at Weihai, Weihai 264209, People's Republic of China

[‡]Department of Physics and Astronomy, Rice University, Houston, Texas 77005, United States

Supporting Information

ABSTRACT: The design of efficient visible-light-driven photocatalysts has become a hot topic due to their potential applications in energy and environmental industries. In this work, sandwiched ZnO@Au@Cu_2O nanorod films were prepared on stainless steel mesh substrates in the order of the following steps: electrodeposition, sputtering, and second electrodeposition. The as-synthesized nanocomposites were characterized by X-ray diffraction, field-emission scanning electron microscopy, transmission electron microscopy, and UV−visible spectrophotometry, respectively. Due to their coaxial structure to inhibit the carrier recombination and the localized surface plasmon resonance effect of Au nanoparticles to enhance the visible light absorption, an outstanding visible-light-driven photocatalytic performance is realized. The enhancement magnitude of Au nanoparticles on the catalytic performance of ZnO@Au@Cu_2O was estimated as a function of the Cu_2O loading amount. The corresponding enhancement mechanism was also explained according to the photocatalytic results under monochromatic visible light irradiation, the active species trapping experiments, and discrete dipole approximation simulation results.

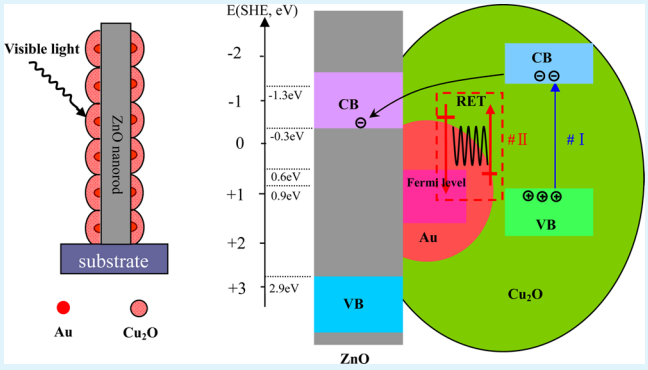

KEYWORDS: *plasmonic photocatalyst, ZnO@Au@Cu_2O nanorod, resonant energy transfer mechanism, electrodeposition*

INTRODUCTION

Although great progress has been made, photocatalysis still suffers from many difficulties, two of which are the low photocatalytic efficiency and the lack of visible-light-driven photocatalytic materials. The former one is mainly due to the serious recombination of charge carriers, while the latter one is due to the wide band gap of the high-performance photocatalytic materials (e.g., TiO_2, ZnO),[1,2] which hinders their applications in the visible light region. How to enhance the visible light absorption and inhibit carrier recombination is therefore the research focus in photocatalyst synthesis. The design of the heterostructure with narrow-band-gap semiconductors is a feasible scheme to solve these problems.[3,4] But after comprehensive consideration of many factors, such as the band gap, the stability of photochemical properties, and the band alignment with the above wide-band-gap ZnO or TiO_2, it is still a challenging task to seek appropriate narrow-band-gap semiconductors. In our early work, Cu_2O has shown to be a satisfactory visible photosensitizer for nanocomposite photocatalysts (e.g., ZnO@Cu_2O),[4] but its 2.2 eV gap means a considerable portion of visible light cannot be efficiently utilized. Therefore, how to expand its response to long-wavelength visible light, even up to the near-infrared (NIR) band of the solar spectrum, remains a challenging task.

The localized surface plasmon resonance (LSPR) effect of metal nanoparticles (NPs) brings enormous opportunities for designing high-performance plasmonic photocatalysts.[5−12] Due to the easy tuning of LSPR characteristics by the metal type, size, and shape and the surrounding dielectric medium, plasmonic photocatalysts can show high performance in the whole solar spectrum. Based on a similar consideration, the performance of Cu_2O based photocatalysts can be further enhanced by the doping or loading of plasmonic metal NPs,[13] but relevant works are rarely found. Just recently Wu's group reported metal (e.g., Au, Ag)@Cu_2O core−shell plasmonic photocatalysts.[14,15] But the serious recombination of the photogenerated e^-−h^+ pairs in Cu_2O still exists, which is particularly fatal for Cu_2O due to its short minority carrier transport length.[16] The introduction of semiconductor heterostructure into plasmonic photocatalysts is expected to gain the optimal photocatalytic performance via the joint contribution of the heterostructure to efficiently inhibit the carrier recombination and LSPR effect to enhance visible light absorption.[17] To the best of our knowledge, there are no relevant reports about the Cu_2O based ternary plasmonic photocatalyst. Meanwhile, the above slurry photocatalysts suffer from particle aggregation and laborious procedures for catalyst recycle, which hinders their practical applications. Therefore,

Received: November 7, 2014
Accepted: February 4, 2015
Published: February 11, 2015

ACS Publications © 2015 American Chemical Society

DOI: 10.1021/am507813g
ACS Appl. Mater. Interfaces 2015, 7, 4066−4074

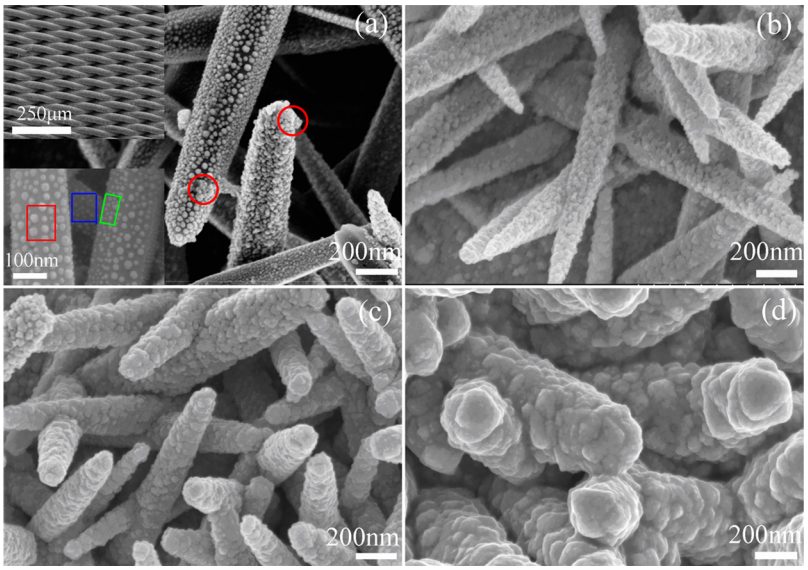

Figure 1. SEM images of ZnO@Au@Cu_2O with Cu_2O deposition for (a) 1, (b) 5, (c) 10, and (d) 40 min. The upper-left and bottom-left insets in panel a are SEM images of the mesh substrate and Au NPs on ZnO nanorods, respectively.

how to prepare supported photocatalysts with high efficiency is particularly important,[18] which is another issue to be considered.

In this work, sandwiched ZnO@Au@Cu_2O nanorod films were synthesized on stainless steel mesh substrates. They exhibited better visible-light photocatalytic performance than the corresponding mono- or bicomponent ones due to their coaxial structure to inhibit carrier recombination and the LSPR effect of Au NPs to enhance visible light absorption. The porous structure of steel mesh substrates also helps in obtaining the high photocatalytic performance. The enhancement mechanism of Au NPs was also estimated according to the photocatalytic results under monochromatic light irradiation, active species trapping experiments, and discrete dipole approximation simulation results.

EXPERIMENTAL SECTION

Synthesis of Sandwiched ZnO@Au@Cu_2O Nanorod Films. The synthesis procedure mainly involves three steps. First, ZnO nanorod films were prepared according to our previously reported procedure.[4] Briefly, a 5 mM aqueous solution of $Zn(NO_3)_2$ and hexamethylene was used as the precursor. A piece of 1 cm × 5 cm stainless steel mesh substrate acted as the cathode to deposit ZnO nanorods at a current density of 0.25 mA/cm^2, with equal area FTO conductive glass as the counter electrode. The experiment was performed for 1 h at 363 K.

Second, Au NPs were sputtered on ZnO nanorods to form ZnO@Au nanostructure. During the dc ion sputtering process (SBC-12, KYKY), the ZnO substrate was 5 cm from the Au target. The discharge current was 8 mA and sputtering time was 30 s for both sides of the substrate. The samples were then annealed at 673 K in air for 60 min to form the discrete distribution of Au NPs.

Third, Cu_2O NPs were then electrodeposited on ZnO@Au substrates to form sandwiched ZnO@Au@Cu_2O. In a typical procedure, the aqueous solution of 0.4 M $CuSO_4$ and 3 M lactic acid was used as the precursor and its pH was adjusted to 12.5 by 5 M NaOH solution. Cu_2O NPs were deposited galvanostatically on the cathode at a current density of 0.9 mA/cm^2 at 313 K for a certain time. Bare ZnO nanorod film or ZnO@Au one acts as the substrate to synthesize ZnO@Cu_2O or ZnO@Au@Cu_2O, respectively.

Characterizations of the Products. The morphologies and structures of the products were characterized by field emission scanning electron microscopy (SEM, Hitachi S-4800) and transmission electron microscopy (TEM, JEOL JEM-2100F). The X-ray diffraction patterns were characterized by an X-ray diffractometer (XRD, Shimadzu XRD-6000) using Cu Kα radiation (λ = 1.5418 Å). The UV−visible light absorption spectra were recorded on a UV−vis spectrophotometer (UV1800, SHIMADU).

Measurement of Photocatalytic Activity under Visible and Monochromatic Light Irradiation. The photocatalytic activity was estimated by degrading 20 mL of methyl orange (MO, 20 mg/L) aqueous solution at room temperature. A solar simulator (Bos-X350-Z, AM) was used as a light source with an intensity of 60 mW/cm^2. The short wavelength light (<400 nm) was cut off by a filter. A 4 cm^2 sample of the ZnO@Au@Cu_2O film was immersed into the MO solution in the dark for 30 min for the sufficient absorption of MO molecules on the surface of the photocatalyst. Absorption spectra of the MO solution were measured using the UV−vis spectrophotometer every 1 h in a total duration of 4 h. The photocatalytic activity was estimated by the change of the peak intensity at 465 nm. The same procedure was followed for the wavelength-dependent photocatalytic test except the light source was coupled to a monochromator. For comparison, the photocatalytic activity of mono- or bicomponent photocatalysts was also measured under identical conditions.

Active Species Trapping Experiments. To detect the active species involved in the photocatalytic process, holes (h^+), hydroxyl radicals (*OH), and superoxide radical ($O_2^{\bullet-}$) were tested by adding 1.0 mM triethanolamine (TEOA, a quencher of h^+),[19,20] isopropyl alcohol (IPA, a quencher of *OH),[21−23] and *p*-benzoquinone (BQ, a quencher of $O_2^{\bullet-}$)[24,25] to the MO solution during the photocatalytic process, respectively. The change of MO absorption spectra by the addition of quenchers was used to determine the active species.

Discrete Dipole Approximation Simulations. To estimate the interaction between Au NPs with neighboring semiconductors (ZnO and Cu_2O), the distribution of the local electromagnetic field in ZnO@Au@Cu_2O was simulated using the free program DDSCAT.[26] The input source was linearly polarized light located at 650 nm, corresponding to the LSPR peak of Au NPs in ZnO@Au@Cu_2O.

RESULTS AND DISCUSSION

The SEM image and XRD pattern of as-synthesized ZnO nanorod film can be found in Figure S1 in the Supporting Information. After electrodeposition for 1 h, dense ZnO nanorods are nearly perpendicularly aligned with a regular hexagonal shape of the cross section, and show an obvious size

DOI: 10.1021/am507813g
ACS Appl. Mater. Interfaces 2015, 7, 4066−4074

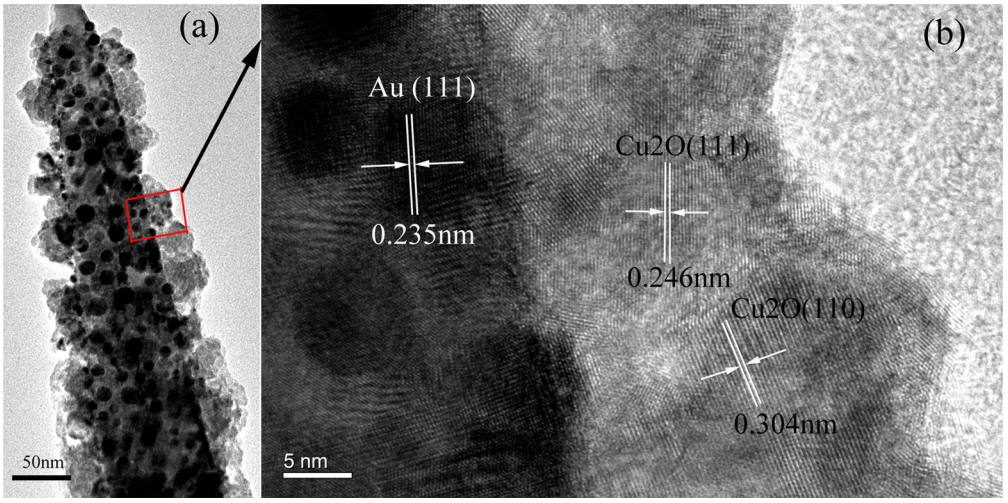

Figure 2. (a) TEM image of the upper part of a ZnO@Au@Cu_2O-5min nanorod and (b) HRTEM image for the interface region marked with a red box.

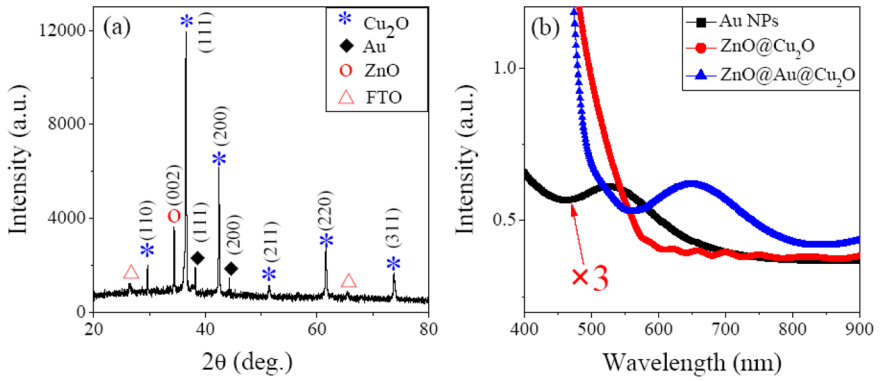

Figure 3. (a) XRD patterns of ZnO@Au@Cu_2O-40 min; (b) UV−vis absorption spectra of Au NPs, ZnO@Cu_2O-5min, and ZnO@Au@Cu_2O-5min.

distribution in diameter. The XRD pattern indicates the formation of hexagonal wurtzite structure of ZnO (JCPDS 36-1451). As shown in the bottom-left inset in Figure 1a, after sputtering and annealing of the Au film, Au NPs are formed and show different distribution characteristics in different positions of ZnO nanorods: large NPs on the top of ZnO nanorods (marked with a red box) and small NPs on the side wall of ZnO and the top of the bottom ZnO nanorod (marked with green and blue boxes, respectively). For the accurate assessment of the size distribution of Au NPs, an SEM image containing more Au NPs and their diameter distribution histogram are presented in Figure S2 in the Supporting Information. The histogram further confirms this distinct distribution characteristic of Au NPs. This distribution difference of Au NPs stems from the uneven topography of the substrate. During sputtering of the Au film, due to the larger exposure area, the Au film on the top of the ZnO nanorod is thicker than that on the side wall and the bottom ZnO nanorods, which leads to this different distribution of Au NPs after annealing. The upper-left inset in Figure 1a shows the porous structure of mesh substrates. For convenience, ZnO@Au@Cu_2O with Cu_2O deposition for 1 min is marked as ZnO@Au@Cu_2O-1min. The notation is also applicable to ZnO@Cu_2O. Without special notification, the above notation remains unchanged in latter context. ZnO@Au@Cu_2O shows apparent change in morphologies as a function of Cu_2O deposition time. For ZnO@Au@Cu_2O-1min, only a few Cu_2O NPs can be found (marked with red circles in Figure 1a), which means 1 min is too short for Cu_2O NPs to effectively nucleate, grow, and absorb on the ZnO@Au surface. For ZnO@Au@Cu_2O-5min and -10min, discrete Cu_2O NPs are covered on ZnO@Au surface to form the core−shell structure (Figure 1b,c). The coaxial structure means a very short distance for photogenerated carriers in Cu_2O to reach the ZnO/Cu_2O interface in the radial direction, which can efficiently inhibit the carrier recombination, especially for Cu_2O due to its short minority carrier transport length.[16] Meanwhile, ZnO nanorods act as an excellent dispersant to inhibit the formation of bigger Cu_2O NPs, which can also efficiently inhibit the carrier recombination.[4] For Cu_2O deposition for 40 min, the submicrometer Cu_2O particles are densely covered on the ZnO@Au surface and the porosity between ZnO nanorods obviously decreases (Figure 1d).

TEM was also employed to characterize the ZnO@Au@Cu_2O nanocomposite (Figure 2). The distribution of Au NPs on ZnO nanorods remains intact even after being covered with Cu_2O NPs (Figure 2a). The size distribution of ZnO@Au@Cu_2O-5min nanorods can be seen in Figure S3 in the Supporting Information. Because the diameter of ZnO@Au@Cu_2O-5min nanorods is gradually reduced at the top part along with its growth direction, we take the measurement position at 420 nm from the top part, and the diameter of one nanorod in the TEM image is 158 nm. For comparisons, five ZnO@Au@

DOI: 10.1021/am507813g
ACS Appl. Mater. Interfaces 2015, 7, 4066−4074

Cu_2O-5min nanorods in the SEM image are also selected to estimate their diameter distribution, and their diameters at 420 nm from the top vary from 150 to 181 nm. The size distribution of different ZnO@Au@Cu_2O-5min nanorods is mainly due to the diameter size distribution of bare ZnO nanorods. In the high-resolution TEM image of the selected interface region (Figure 2b), the lattice fringes with a spacing of 0.235 nm are assigned to the interplanar spacing of the (111) crystal plane of Au NPs. The lattice fringes with spacings of 0.246 and 0.304 nm are assigned to the interplanar spacings of the (111) and (110) crystal planes of Cu_2O. The lattice fringes of ZnO nanorods cannot be found for the thick coverage of Au NPs and Cu_2O shell.

The phases of ZnO@Au@Cu_2O nanocomposite are shown in Figure 3a. Several strong diffraction peaks, corresponding to that of the cubic phase Cu_2O (JCPDS 65-3288), are identified for the (110), (111), (200), (211), (220), and (311) lattice planes, respectively. Except for the peaks of Cu_2O, the diffraction peaks of ZnO and Au are relatively weak due to the coverage with a thick Cu_2O shell. The peak located at 34.4° can be indexed to the (002) lattice plane of ZnO. The peaks located at 38.2 and 44.3° can be indexed to the (111) and (200) lattice planes of Au, respectively. The minuscule peaks located at 26.5 and 65.5° were indexed to the FTO substrate.

To measure the UV−visible absorption spectra of ZnO@Au@Cu_2O-5min and ZnO@Cu_2O-5min, they were deposited on FTO substrates under identical conditions, respectively, and the obtained absorption spectra are shown in Figure 3b. For ZnO@Cu_2O, the absorption edge at 2.2 eV is due to the interband absorption of Cu_2O. For ZnO@Au@Cu_2O, a broad absorption peak located at 650 nm is assigned to LSPR absorption of Au NPs. The apparent red shift of the LSPR peak from 525 nm of bare Au NPs is due to the coverage with high-refractive-index Cu_2O shell.[11] The UV−visible spectra clearly show an LSPR red shift and broadening correlated with increasing Cu_2O deposition time (Figure S4 in the Supporting Information). It should be noted that the broad LSPR peak is beneficial for ZnO@Au@Cu_2O to harvest the visible light as much as possible.

The photocatalytic results of the ZnO@Au@Cu_2O and the other reference photocatalysts are shown in Figure 4. The trend in their photocatalytic activities follows the order ZnO@Au@Cu_2O > Au@Cu_2O > ZnO@Cu_2O > Cu_2O > ZnO@Au > ZnO > Au. The following several points can be drawn according to the comparison results of catalytic activities. First, ZnO@Cu_2O shows a pronounced photocatalytic activity, mainly due to the visible-light-responsive characteristic of Cu_2O and its energy band matching well with that of ZnO.[4] Second, Au NPs significantly improve the visible-light photocatalytic activities of Cu_2O and ZnO. Third, the sandwiched ZnO@Au@Cu_2O shows the optimal photocatalytic performance due to the synergistic effect of Au NPs and the ZnO/Cu_2O heterogeneous structure. The enhancement mechanism of Au NPs on the photocatalysis will be discussed in detail later. It has been reported that LSPR-mediated local heating effect could lead to the thermochemical degradation of organic molecules.[27,28] To judge if the heating effect is responsible for the photocatalytic improvement of Au NPs, Au NPs were deposited on the quartz glass under identical conditions. The bare Au NPs showed no photocatalytic activity, which could rule out the thermal activation effect.

Compared with the conventional semiconductor photocatalysis, plasmonic photocatalysis possesses two distinct

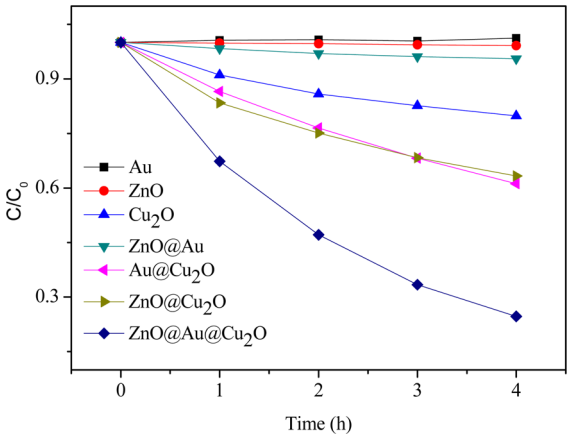

Figure 4. Visible-light degradation of MO versus time in the presence of photocatalysts. The deposition time of Cu_2O is 5 min for all samples. C_0 and C refer to the initial absorption peak intensity of MO solution and that after light irradiation for a certain time, respectively. Note that, without special notification, C_0 and C have the same meaning in the latter context.

features: the Schottky junction and the LSPR effect. To determine which is responsible for the photocatalytic improvement of Au NPs in ZnO@Au@Cu_2O, the monochromatic photocatalysis action spectra of ZnO@Au@Cu_2O and ZnO@Cu_2O were normalized to the unit power of incident monochromatic light and plotted versus the wavelength of light irradiation, as shown in Figure 5. The absorption spectra are also presented in Figure 5 for comparison. The power of monochromatic light can be found in the Supporting Information (Table S1). For ZnO@Cu_2O, the photocatalytic action spectrum follows its absorption spectrum. When the monochromatic light is below the band edge of Cu_2O, its catalytic activity quickly drops to zero. For ZnO@Au@Cu_2O, the action spectrum also follows its absorption spectrum with obvious enhancement at the LSPR region in comparison with ZnO@Cu_2O. The highest activity is observed at wavelengths at which Au NPs strongly absorb light. Clearly, the light absorbed by Au NPs is the driving force of photocatalytic reactions. It should be noted that the response of ZnO@Au@Cu_2O was extended to the NIR region by LSPR-induced absorption of Au NPs. (Note: The 808 nm monochromatic light is the longest wavelength one we can acquire.)

Now we estimate the contribution of the LSPR effect of Au NPs on the whole photocatalytic performance of ZnO@Au@Cu_2O. As shown in Figure 5b, under the unit power monochromatic light irradiation, the degradation efficiency $((C_0 - C)/C_0)$ in the LSPR region of Au NPs is comparable to or even more than that in the Cu_2O absorption region (e.g., at 476 nm). Considering the enormous broadening of the LSPR peak of Au NPs in ZnO@Au@Cu_2O photocatalysts, it is reasonable to argue that the contribution of the LSPR effect of Au NPs is comparable to or even more than that of Cu_2O under the natural solar irradiation.

For ZnO@Cu_2O samples, more Cu_2O loading leads to the better photocatalytic performance when the deposition time of Cu_2O is less than 30 min (Figure S5 in the Supporting Information), which is consistent with our previous results.[4] The impact of Cu_2O loading amount on the catalytic activity of ZnO@Au@Cu_2O samples is also investigated by varying the deposition time of Cu_2O while maintaining other experimental conditions unchanged, and the results are shown in Figure 6a.

DOI: 10.1021/am507813g
ACS Appl. Mater. Interfaces 2015, 7, 4066−4074

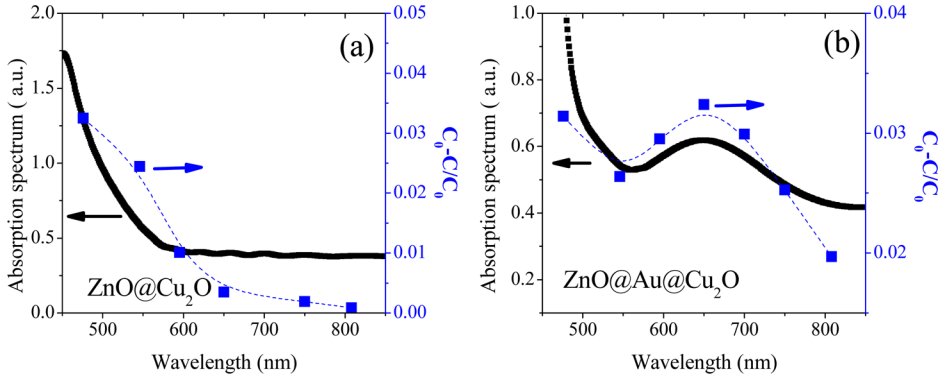

Figure 5. UV−visible absorption spectra and normalized photocatalytic action spectra for (a) ZnO@Cu_2O-5min and (b) ZnO@Au@Cu_2O-5min under monochromatic visible light irradiation for 1 h.

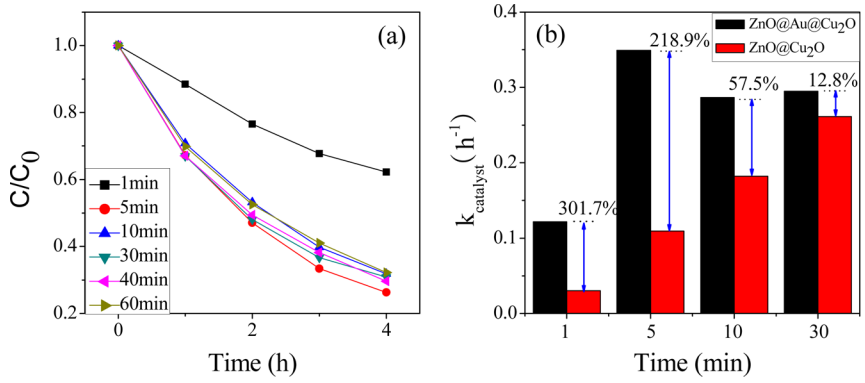

Figure 6. (a) Visible-light photodegradation of MO versus time in the presence of ZnO@Au@Cu_2O with different Cu_2O deposition times. (b) Apparent reaction rate constants of ZnO@Au@Cu_2O and ZnO@Cu_2O samples as a function of Cu_2O deposition time under visible light irradiation. The enhancement factor is defined as $[(k_{ZnO@Au@Cu_2O} - k_{ZnO@Cu_2O})/k_{ZnO@Cu_2O}]\cdot 100\%$, and the magnitude is correspondingly listed in panel b.

It is of great interest that the Cu_2O loading amount has no obvious effect on the photocatalytic ability of ZnO@Au@Cu_2O. ZnO@Au@Cu_2O-1min is the only exception, which may be due to the inadequate Cu_2O NP formation on the ZnO@Au surface, as shown in Figure 1a. The distinct tread of the photocatalytic performance of ZnO@Au@Cu_2O and ZnO@Cu_2O as a function of Cu_2O loading amount again certifies that Au NPs play a key role in the ternary photocatalyst.

The degradation of MO in the presence of ZnO@Au@Cu_2O or ZnO@Cu_2O composite photocatalysts can be ascribed to a pseudo-first-order reaction with the Langmuir−Hinshelwood model, and the obtained apparent reaction rate constants (k) can be found in Table S2 in the Supporting Information and in Figure 6b. As can be seen, the existence of Au NPs significantly improves the catalytic performance of ZnO@Au@Cu_2O, but the enhancement magnitude correspondingly reduces from 301.7 to 12.8% with the increase of Cu_2O deposition time from 1 to 30 min. More Cu_2O loading in ZnO@Au@Cu_2O restrains the photocatalytic enhancement of Au NPs, which will be discussed in the latter.

The active species trapping experiment results in the presence of ZnO@Au@Cu_2O are shown in Figure S6 in the Supporting Information. It can be found that the addition of BQ has no effect on the photocatalytic activity of ZnO@Au@Cu_2O. However, the separate addition of TEOA or IPA leads to the entire or partial inactivation of ZnO@Au@Cu_2O. The above results indicate that the h^+ and the resultant *OH are the main active species involved in the photocatalytic process.

The LSPR effect of metal NPs can distinctly improve the photocatalysis of semiconductors, but the enhancement mechanism remains controversial. Direct electron transfer (DET) from metal NPs to the semiconductor is possible when they are in direct contact with each other, but the DET mechanism requires the simultaneous transfer of compensative electrons from the donor to metal NPs.[10,29] SPR-mediated extensive local electromagnetic field (LEMF) can also enhance the photocatalysis via exciting more e^-−h^+ pairs in the neighboring semiconductor, but the prerequisite is larger plasmon energy than the band gap of semiconductors.[30−34] Just recently Wu et al. proposed a resonant energy transfer mechanism (RET) as the reasonable explanation for the enhanced photocatalytic performance of Au@Cu_2O.[15] Under the plasmon excitation in Au NPs, e^-−h^+ pairs can be generated in Cu_2O via resonant energy transfer from the LSPR dipole to the e^-−h^+ pair, similar to the Förster resonance energy transfer process. RET can only take place when the adsorption edge of Cu_2O and the LSPR peak of Au NPs partially overlap, and is directly proportional to the degree of their overlap. The absorption of Cu_2O drops gradually but not drastically in the visible light region less than its band gap. Meanwhile, the significant broadening of the LSPR peak of Au NPs in Au@Cu_2O results in their partial overlap, so Au@Cu_2O can still show efficient photocatalytic performance under visible light irradiation with energy less than the band gap of Cu_2O.

The transfer process of energy or electrons in the ternary ZnO@Au@Cu_2O is more complicated than in the corresponding binary one. To understand the photocatalysis process, two

DOI: 10.1021/am507813g
ACS Appl. Mater. Interfaces 2015, 7, 4066−4074

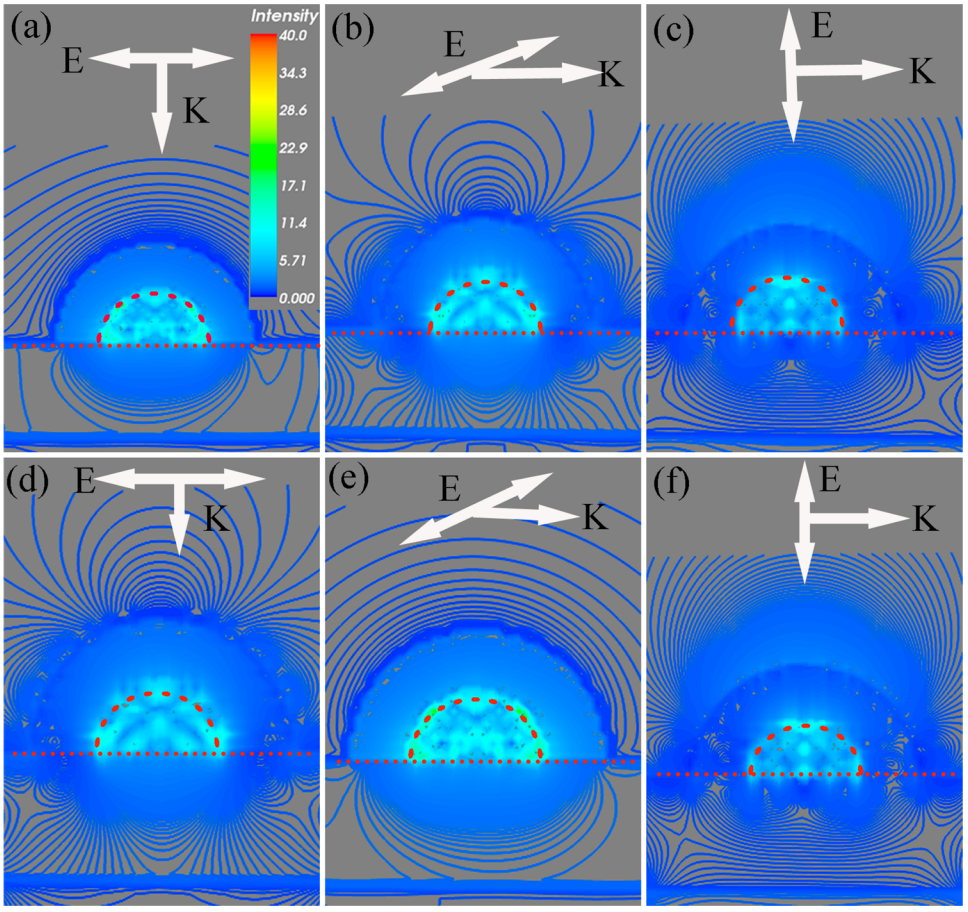

Figure 7. Distribution of the local electromagnetic field of the ZnO@Au@Cu_2O nanostructure under visible light irradiation. In the simulation, the hemispherical Au core−Cu_2O shell is located on ZnO substrate. Through the TEM image in Figure 2a, we can see the thickness of the Cu_2O shell in ZnO@Au@Cu_2O-5min varies from 0 to 10 nm, even up to 25 nm, and the largest distribution of thickness appears around 10 nm, so we take 10 nm thickness for instance in our simulations. The 650 nm wavelength of the incident linearly polarized light corresponds to the strongest LSPR region of ZnO@Au@Cu_2O-5min. The incident and polarization directions are marked with "K" and "E", respectively. Panels a and d correspond to incidence along the *z* axis and polarization along the *y* axis. Panels b and e correspond to incidence along the *y* axis and polarization along the *x* axis. Panels c and f correspond to incidence along the *y* axis and polarization along the *z* axis. Two panels in every column correspond to the field distribution in the slices perpendicular to each other with the identical incidence and polarization directions. The interfaces of three components are marked with the red dotted lines. All panels share the identical color scale in panel a.

questions must be answered: (1) Which mechanism dominates the photocatalytic enhancement of Au NPs? (2) Do active electrons or energy transfer from Au NPs to ZnO or Cu_2O? On the first question, effective coverage of Au NPs by Cu_2O shell hinders the compensation channel of electrons from MO solution, which rules out the DET mechanism.[10,35] Meanwhile, the smaller plasmon energy of Au NPs in ZnO@Au@Cu_2O than the band gap of Cu_2O also excludes the LEMF mechanism. The RET mechanism can be used to reasonably explain our experimental results. On the second question, because the generation rate of e^-−h^+ pairs in semiconductors is proportional to the intensity of the local electromagnetic field,[36,37] the distribution of the local field can indicate the main transfer path of plasmon energy. The corresponding discrete dipole approximation simulation results can be seen in Figure 7. The schematic architecture of the ZnO@Au@Cu_2O model and adoptive coordinate system can be seen in Figure S7 in the Supporting Information. As shown in Figure 7, with incidence along the *z* axis and polarization along the *y* axis, the electromagnetic field is mainly located in the Au−Cu_2O interface (7a,d). With incidence along the *y* axis and polarization along the *x* axis, a similar field distribution is obtained (7b,e). With incidence along the *y* axis and polarization along the *z* axis, the strongest field is distributed in the Au−Cu_2O interface along the *z* axis (7c,f). The stronger local field in 7Au/Cu_2O interface under light irradiation with various polarization and incidence directions means the RET process mainly occurs between Au and Cu_2O. It should be noted that the partial permeation of the electromagnetic field into Cu_2O (Figure 7b,d,f) can enormously boost the generation of charge carriers in Cu_2O via the RET process.

The influence of Cu_2O thickness on the field distribution of ZnO@Au@Cu_2O is estimated by varying the thickness of the Cu_2O shell while maintaining other parameters unchanged (Figure S8 in the Supporting Information). The local electromagnetic field gradually weakens along with the increase of the thickness of Cu_2O shell under 650 nm light irradiation with various polarization and incidence directions, which means the coverage of Au NPs with thicker Cu_2O reduces its contribution to the catalytic activity. Meanwhile, the thickening of Cu_2O shell can result in two adverse effects: One is the more serious recombination of LSPR-initiated carriers in Cu_2O. The other is that less overlap between the SPR peak of Au NPs and band gap of Cu_2O leads to less carrier generation via the RET

DOI: 10.1021/am507813g
ACS Appl. Mater. Interfaces 2015, 7, 4066−4074

process. The above analysis can reasonably explain the results in Figure 6.

MO has been widely used as model molecules of organic pollutants in photocatalytic processes. It can be efficiently degraded by the photogenerated charge carriers in ZnO/Cu_2O and Au/Cu_2O composite photocatalysts.[4,14,15] According to the above analysis, the generation and transfer process of charge carriers in ZnO@Au@Cu_2O is shown in Figure 8. For ZnO@Au@Cu_2O samples, Cu_2O and Au NPs are both photosensitive elements under the visible light irradiation. e^-–h^+ pairs can be generated in Cu_2O via the interband excitation (#I process). Meanwhile, the obtained energy in Au NPs via LSPR absorption can be transferred to the neighboring Cu_2O to initiate active e^-–h^+ pairs (RET process, #II process), so the photocatalytic performance of ZnO@Au@Cu_2O samples is determined by the combination of the above two process. The generated active electrons in Cu_2O via the above two processes will be preferentially injected into the conduction band of ZnO, rather than directly react with MO molecules considering the tremendous difference of the electron transfer time constants of the above two processes.[30,38] The accumulated electrons in ZnO cannot reduce O_2 to $O_2^{\bullet-}$ through a one-electron reaction process for the inadequate reduced potential ($O_2 + e^- \rightarrow O_2^{\bullet-}$; $(O_2/O_2)^{\bullet-}$ −0.33 eV vs NHE).[39] The trapping experiment of BQ quencher can also indirectly support the above viewpoint. The photogenerated holes in Cu_2O can degrade MO molecules via direct oxidation or the formation of intermediates *OH species, so the holes and the resultant *OH are the main active species involved in the photodegradation process, which is consistent with the active species trapping experiment results.

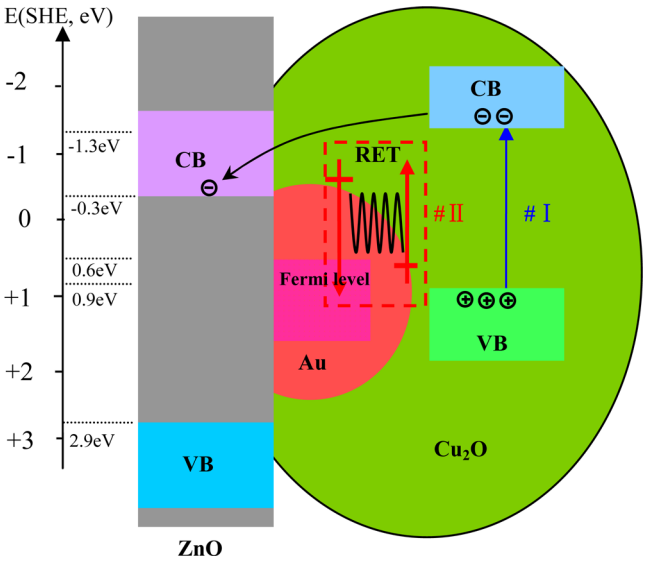

Figure 8. Schematic representation of the generation and transfer of charge carriers in ZnO@Au@Cu_2O under visible light irradiation. #I refers to interband excitation in Cu_2O, and #II refers to RET-initiated carrier generation in Cu_2O.

For the above-mentioned #I and #II processes, with the increase of Cu_2O loading amount, the #I process enhances the photocatalytic performance of ZnO@Au@Cu_2O samples due to the stronger visible light absorption of Cu_2O, and a similar variation trend of ZnO@Cu_2O as a function of Cu_2O deposition time can be seen in Figure S5 in the Supporting Information. On the contrary, due to the decrease of local EM field along with the increase of Cu_2O thickness, the #II process weakens the photocatalytic performance of ZnO@Au@Cu_2O samples. In fact, it is because these two effects are opposite to each other that there will be a maximum photocatalytic performance with increasing Cu_2O loading amount, just as seen in the behavior of ZnO@Au@Cu_2O with Cu_2O deposition time increasing from 5 to 60 min, as shown in Figure 6a.

Last, we would emphasize the advantage of ZnO@Au@Cu_2O structure upon the photocatalytic performance. First, the coaxial structure means a very short distance for photogenerated carriers to transfer and separate in the ZnO/Cu_2O interface, which can efficiently inhibit the carrier recombination. Second, the LSPR effect of Au NPs in ZnO@Au@Cu_2O nanocomposites can broaden their photocatalytic response to the whole visible light region, even up to the NIR region. The normalized monochromatic catalytic results in Figure 5b indicate the contribution of the LSPR effect of Au NPs is comparable to or even more than that of Cu_2O. Last, the as-synthesized ZnO@Au@Cu_2O shows great potential in the environmental and energy industries for many advantages, such as the low cost and massive production ability, the application of flexible porous mesh substrates, and the supported form of photocatalysts in favor of the catalyst recycle.

CONCLUSIONS

In summary, sandwiched ZnO@Au@Cu_2O nanorod films were synthesized on steel mesh substrates via a simple three-step approach. Benefiting from their coaxial structure to inhibit the carrier recombination and the LSPR effect of Au NPs to enhance the visible light absorption, the as-synthesized nanocomposites show an efficient visible-light photocatalytic performance for the degradation of the MO solution. The Au NPs sandwiched between ZnO and Cu_2O greatly improve the catalytic performance of ZnO@Cu_2O, but the enhancement magnitude significantly decreases with the increase of the Cu_2O shell thickness. For ZnO@Au@Cu_2O, active e^-–h^+ pairs are generated in Cu_2O via the interband excitation and resonant energy transfer from the local plasmon dipole of Au NPs. The rapid separation of e^-–h^+ pairs in the Cu_2O/ZnO interface guarantees the high performance of ZnO@Au@Cu_2O. With the increase of Cu_2O loading in ZnO@Au@Cu_2O, the damping of the local electromagnetic field in the Au/Cu_2O interface and the more serious recombination of carriers in Cu_2O result in the partial inactivation of ZnO@Au@Cu_2O. The present work provides a low-cost but efficient solution for the large scale production of satisfactory visible-light-responsive photocatalysts.

ASSOCIATED CONTENT

Supporting Information

SEM image and XRD pattern of bare ZnO nanorod film; SEM image and diameter distribution histogram of Au NPs; diameter distribution of ZnO@Au@Cu_2O-5min nanorods; absorption spectra of ZnO@Au@Cu_2O as a function of Cu_2O deposition time; wavelength of monochromatic light and corresponding power used in photocatalytic tests under monochromatic light; photodegradation of MO in the presence of as-prepared ZnO@Cu_2O samples with different Cu_2O deposition times under visible light irradiation; apparent reaction rate constants of ZnO@Au@Cu_2O and ZnO@Cu_2O samples for MO photodegradation; trapping experiment of active species during photodegradation of MO in the presence of ZnO@Au@Cu_2O samples; schematic architecture of ZnO@Au@Cu_2O nano-

DOI: 10.1021/am507813g
ACS Appl. Mater. Interfaces 2015, 7, 4066−4074

composites and adoptive coordinate system; intensity distribution of local electromagnetic field in ZnO@Au@Cu_2O nanosystem as a function of the thickness of Cu_2O shell. This material is available free of charge via the Internet at http://pubs.acs.org.

AUTHOR INFORMATION

Corresponding Author

*E-mail: rstian600@sohu.com.

Notes

The authors declare no competing financial interest.

ACKNOWLEDGMENTS

We are thankful for the financial support by the Natural Scientific Research Innovation Foundation in Harbin Institute of Technology (HIT. NSRIF. 2015104), Weihai Campus Discipline Construction Pilot Foundation (WH20140204) and National Natural Science Foundation of China (Grant Nos. 11274082).

REFERENCES

(1) Hashimoto, K.; Irie, H.; Fujishima, A. TiO_2 Photocatalysis: a Historical Overview and Future Prospects. *Jpn. J. Appl. Phys.* **2005**, *44*, 8269−8285.

(2) Behnajady, M. A.; Modirshahla, N.; Hamzavi, R. Kinetic Study on Photocatalytic Degradation of C.I. Acid Yellow 23 by ZnO Photocatalyst. *J. Hazard. Mater.* **2006**, *B133*, 226−232.

(3) Kundu, P.; Deshpande, P. A.; Madras, G.; Ravishankar, N. Nanoscale ZnO/CdS Heterostructures with Engineered Interfaces for High Photocatalytic Activity under Solar Radiation. *J. Mater. Chem.* **2011**, *21*, 4209−4216.

(4) Ren, S. T.; Fan, G. H.; Liang, M. L.; Wang, Q.; Zhao, G. L. Electrodeposition of Hierarchical ZnO/Cu_2O Nanorod Films for Highly Efficient Visible-Light-Driven Photocatalytic Applications. *J. Appl. Phys.* **2014**, *115*, 064301.

(5) Awazu, K.; Fujimaki, M.; Rockstuhl, C.; Tominaga, J.; Murakami, H.; Ohki, Y.; Yoshida, N.; Watanabe, T. A Plasmonic Photocatalyst Consisting of Silver Nanoparticles Embedded in Titanium Dioxide. *J. Am. Chem. Soc.* **2008**, *130*, 1676−1680.

(6) Wang, P.; Huang, B.; Dai, Y.; Whangbo, M.-H. Plasmonic Photocatalysts: Harvesting Visible Light with Noble Metal Nanoparticles. *Phys. Chem. Chem. Phys.* **2012**, *14*, 9813.

(7) Jiang, J.; Li, H.; Zhang, L. New Insight into Daylight Photocatalysis of AgBr@Ag: Synergistic Effect between Semiconductor Photocatalysis and Plasmonic Photocatalysis. *Chem.—Eur. J.* **2012**, *18*, 6360−6369.

(8) Linic, S.; Christopher, P.; Ingram, D. B. Plasmonic-Metal Nanostructures for Efficient Conversion of Solar to Chemical Energy. *Nat. Mater.* **2011**, *10*, 911−921.

(9) Zhang, N.; Liu, S.; Xu, Y.-J. Recent Progress on Metal Core@Semiconductor Shell Nanocomposites as a Promising Type of Photocatalyst. *Nanoscale* **2012**, *4*, 2227−2238.

(10) Tian, Y.; Tatsuma, T. Mechanisms and Applications of Plasmon-Induced Charge Separation at TiO_2 Films Loaded with Gold Nanoparticles. *J. Am. Chem. Soc.* **2005**, *127*, 7632−7637.

(11) Kumar, M. K.; Krishnamoorthy, S.; Tan, L. K.; Chiam, S. Y.; Tripathy, S.; Gao, H. Field Effects in Plasmonic Photocatalyst by Precise SiO_2 Thickness Control Using Atomic Layer Deposition. *ACS Catal.* **2011**, *1*, 300−308.

(12) Chen, K.; Pu, Y.; Chang, K.; Liang, Y.; Liu, C.; Yeh, J.; Shih, H.; Hsu, Y. Ag-Nanoparticle-Decorated SiO_2 Nanospheres Exhibiting Remarkable Plasmon-Mediated Photocatalytic Properties. *J. Phys. Chem. C* **2012**, *116*, 19039−19045.

(13) Liu, D.; Ding, S.; Lin, H.; Liu, B.; Ye, Z.; Fan, F.; Ren, B.; Tian, Z. Distinctive Enhanced and Tunable Plasmon Resonant Absorption from Controllable Au@Cu_2O Nanoparticles: Experimental and Theoretical Modeling. *J. Phys. Chem. C* **2012**, *116*, 4477−4483.

(14) Li, J.; Cushing, S. K.; Bright, J.; Meng, F.; Senty, T. R.; Zheng, P.; Bristow, A. D.; Wu, N. Ag@Cu_2O Core-Shell Nanoparticles as Visible-Light Plasmonic Photocatalysts. *ACS Catal.* **2013**, *3*, 47−51.

(15) Cushing, S. K.; Li, J.; Meng, F.; Senty, T. R.; Suri, S.; Zhi, M.; Li, M.; Bristow, A. D.; Wu, N. Photocatalytic Activity Enhanced by Plasmonic Resonant Energy Transfer from Metal to Semiconductor. *J. Am. Chem. Soc.* **2012**, *134*, 15033−15041.

(16) Liu, Y.; Turley, H. K.; Tumbleston, J. R.; Samulski, E. T.; Lopez, R. Minority Carrier Transport Length of Electrodeposited Cu_2O in ZnO/Cu_2O Heterojunction Solar Cells. *Appl. Phys. Lett.* **2011**, *98*, 162105.

(17) Lin, Y. G.; Hsu, Y. K.; Chen, Y. C.; Wang, S. B.; Miller, J. T.; Chen, L. C.; Chen, K. H. Plasmonic Ag@$Ag_3(PO_4)_{1-x}$ Nanoparticle Photosensitized ZnO Nanorod-Array Photoanodes for Water Oxidation. *Energy Environ. Sci.* **2012**, *5*, 8917−8922.

(18) Arabatzis, I. M.; Stergiopoulos, T.; Andreeva, D.; Kitova, S.; Neophytides, S. G.; Falaras, P. Characterization and Photocatalytic Activity of Au/TiO_2 Thin Films for Azo-Dye Degradation. *J. Catal.* **2003**, *220*, 127−135.

(19) Ye, L.; Deng, K.; Xu, F.; Tian, L.; Peng, T.; Zan, L. Increasing Visible-Light Absorption for Photocatalysis with Black BiOCl. *Phys. Chem. Chem. Phys.* **2012**, *14*, 82−85.

(20) Chen, F.; Liu, H.; Bagwasi, S.; Shen, X.; Zhang, J. Photocatalytic Study of BiOCl for Degradation of Organic Pollutants under UV Irradiation. *J. Photochem. Photobiol., A* **2010**, *215*, 76−80.

(21) Ji, P.; Zhang, J.; Chen, F.; Anpo, M. Study of Adsorption and Degradation of Acid Orange 7 on the Surface of CeO_2 under Visible Light Irradiation. *Appl. Catal., B* **2009**, *85*, 148−154.

(22) Bowmaker, G. A.; Pakawatchai, C.; Saithong, S.; Skeltonc, B. W.; White, A. H. Structural and Spectroscopic Studies of some Adducts of Silver(I) Halides with Thiourea and N-ethyl Substituted Thioureas. *Dalton Trans.* **2010**, *39*, 4391−4404.

(23) Zhou, L.; Liu, J.; Liu, Z. J. Adsorption of Platinum(IV) and Palladium(II) from Aqueous Solution by Thiourea-Modified Chitosan Microspheres. *Hazard. Mater.* **2009**, *172*, 439−446.

(24) Khan, S. A.; Singh, N.; Saleem, K. Synthesis, Characterization and in vitro Antibacterial Activity of Thiourea and Urea Derivatives of Steroids. *Eur. J. Med. Chem.* **2008**, *43*, 2272−2277.

(25) Bolzana, A. E.; Iwasita, T.; Arvia, A. J. In situ FTIRRAS Study of the Electro-Oxidation Reactions of Thiourea and Gold in Aqueous Acid Solutions. *J. Electroanal. Chem.* **2003**, *554*−*555*, 49−60.

(26) Draine, B. T.; Flatau, P. J. Discrete-Dipole Approximation for Scattering Calculations. *J. Opt. Soc. Am. A* **1994**, *11*, 1491−1499.

(27) Christopher, P.; Ingram, D. B.; Linic, S. Enhancing Photochemical Activity of Semiconductor Nanoparticles with Optically Active Ag Nanostructures: Photochemistry Mediated by Ag Surface Plasmons. *J. Phys. Chem. C* **2010**, *114*, 9173−9177.

(28) Rycenga, M.; Cobley, C. M.; Zeng, J.; Li, W.; Moran, C. H.; Zhang, Q.; Qin, D.; Xia, Y. Controlling the Synthesis and Assembly of Silver Nanostructures for Plasmonic Applications. *Chem. Rev.* **2011**, *111*, 3669−3712.

(29) Furube, A.; Du, L.; Hara, K.; Katoh, R.; Tachiya, M. Ultrafast Plasmon-Induced Electron Transfer from Gold Nanodots into TiO_2 Nanoparticles. *J. Am. Chem. Soc.* **2007**, *129*, 14852−14853.

(30) Atwater, H. A.; Polman, A. Plasmonics for Improved Photovoltaic Devices. *Nat. Mater.* **2010**, *9*, 205−213.

(31) Liu, Z.; Hou, W.; Pavaskar, P.; Aykol, M.; Cronin, S. B. Plasmon Resonant Enhancement of Photocatalytic Water Splitting under Visible Illumination. *Nano Lett.* **2011**, *11*, 1111−1116.

(32) Ingram, D. B.; Linic, S. Water Splitting on Composite Plasmonic-Metal/Semiconductor Photoelectrodes: Evidence for Selective Plasmon-Induced Formation of Charge Carriers near the Semiconductor Surface. *J. Am. Chem. Soc.* **2011**, *133*, 5202−5205.

(33) Wang, L.; Clavero, C.; Huba, Z.; Carroll, K. J.; Carpenter, E. E.; Gu, D.; Lukaszew, R. A. Plasmonics and Enhanced Magneto-Optics in Core-Shell Co-Ag Nanoparticles. *Nano Lett.* **2011**, *11*, 1237−1240.

DOI: 10.1021/am507813g
ACS Appl. Mater. Interfaces 2015, 7, 4066−4074

(34) Tcherniak, A.; Ha, J. W.; Dominguez-Medina, S.; Slaughter, L. S.; Link, S. Probing a Century Old Prediction: one Plasmonic Particle at a time. *Nano Lett.* **2010**, *10*, 1398−1404.
(35) Yang, L. B.; Jiang, X.; Ruan, W. D.; Yang, J. X.; Zhao, B.; Xu, W. Q.; Lombardi, J. R. Charge-Transfer-Induced Surface-Enhanced Raman Scattering on Ag-TiO_2 Nanocomposites. *J. Phys. Chem. C* **2009**, *113*, 16226−16231.
(36) Lee, J.; Javed, T.; Skeini, T.; Govorov, A. O.; Bryant, G. W.; Kotov, N. A. Bioconjugated Ag Nanoparticles and CdTe Nanowires: Metamaterials with Field-Enhanced Light Absorption. *Angew. Chem., Int. Ed.* **2006**, *45*, 4819−4823.
(37) Lee, S. J.; Morrill, A. R.; Moskovits, M. Hot Spots in Silver Nanowire Bundles for Surface-Enhanced Raman Spectroscopy. *J. Am. Chem. Soc.* **2006**, *128*, 2200−2201.
(38) Chen, Y.; Pu, Y.; Hsu, Y. Interfacial Charge Carrier Dynamics of the Three-Component In_2O_3-TiO_2-Pt Heterojunction System. *J. Phys. Chem. C* **2012**, *116*, 2967−2975.
(39) Zhang, X.; Chen, Y. L.; Liu, R.-S.; Tsai, D. P. Plasmonic Photocatalysis. *Rep. Prog. Phys.* **2013**, *76*, 046401.

DOI: 10.1021/am507813g
ACS Appl. Mater. Interfaces 2015, 7, 4066−4074